SCIENCE CHINA
Information Sciences

• RESEARCH PAPER •

April 2021, Vol. 64 140403:1–140403:8
https://doi.org/10.1007/s11432-020-3179-9

Special Focus on Two-Dimensional Materials and Device Applications

Efficient graphene in-plane homogeneous p-n-p junction based infrared photodetectors with low dark current

Junru AN[1,2], Tian SUN[3,4], Bin WANG[1,2], Jianlong XU[3*] & Shaojuan LI[1,2*]

[1] *State Key Laboratory of Applied Optics, Changchun Institute of Optics, Fine Mechanics and Physics, Chinese Academy of Sciences, Changchun 130033, China;*
[2] *University of Chinese Academy of Sciences (UCAS), Beijing 100049, China;*
[3] *Institute of Functional Nano and Soft Materials (FUNSOM), Jiangsu Key Laboratory for Carbon-Based Functional Materials and Devices, Soochow University, Suzhou 215123, China;*
[4] *Wuhan National Laboratory for Optoelectronics and School of Optical and Electronic Information, Huazhong University of Science and Technology, Wuhan 430074, China*

Received 29 October 2020/Revised 19 January 2021/Accepted 29 January 2021/Published online 8 March 2021

Abstract Graphene-based photodetectors have drawn a large amount of interests owing to its wide spectral response, however, the high dark current greatly limits their applications. In this study, we develop an efficient graphene in-plane homogeneous p-n-p junction based infrared (IR) photodetector with greatly reduced dark current. The devices with p-n-p junctions exhibit excellent photoresponse to 1.0∼4.0 μm IR light illumination with ultra-low dark current at the order of $\sim 10^{-9}$ A in double p-n-p junctions and 10^{-13} A in three p-n-p junctions based photodetector, which is three and seven orders of magnitude lower than pristine graphene phototransistors, respectively. The excellent IR photodetection capabilities could be attributed to the synergistic effects of in-plane photovoltaic effects as well as the photogating effects induced carrier injection from the silicon substrate. Our results suggest intriguing potential of graphene in-plane p-n-p junctions for applications in high-performance IR photodetectors.

Keywords infrared photodetector, graphene, p-n-p junction, dark current, photoresponse

Citation An J R, Sun T, Wang B, et al. Efficient graphene in-plane homogeneous p-n-p junction based infrared photodetectors with low dark current. Sci China Inf Sci, 2021, 64(4): 140403, https://doi.org/10.1007/s11432-020-3179-9

1 Introduction

Graphene-based photodetectors have attracted immerse attention owing to the unique optoelectronic properties of graphene including broadband light absorption, high carrier mobility, mechanical flexibility as well as excellent thermal conductivity [1–3]. Graphene exhibits ultra-broadband light absorption over wavelengths from ultra-violet to the terahertz region, and a rapid photoresponse [4–6], which provides a gigahertz-order (GHz) bandwidth over the infrared (IR) spectrum [7–9]. Moreover, graphene films can be fabricated by a low-cost green method [10, 11], which is in contrast to conventional IR materials [12, 13] such as indium gallium arsenide (InGaAs), gallium arsenide/aluminum gallium arsenide (GaAs/AlGaAs) quantum wells and indium arsenide antimony/aluminum arsenide antimony (InAsSb/AlAsSb) superlattices. Homogeneous graphene p-n junctions are promising candidates to achieve excellent photodetection performances [14–16], because there is no interfacial lattice mismatch and a uniform energy potential profile [17] is formed across the device. It has been reported that the internal quantum efficiency can be enhanced in homogeneous p-n junctions [18, 19], and some unique physical phenomena, such as Klein tunneling effect [20] and Veselago lensing [21], have also been predicted and realized. For building p-n junctions, doping methods including classical interstitial doping [22–24] as well as electrical-gating [25] have been utilized for fabrication of p- or n-type graphene and thus enabling the formation of graphene

* Corresponding author (email: xujianlong@suda.edu.cn, lishaojuan@ciomp.ac.cn)

p-n junctions. Although graphene homogeneous p-n junction based graphene photodetectors exhibits relatively high photoresponsivity, the dark current is usually very high [26–28], arising from the gapless nature of graphene. In such photodetectors, the dark current is always much higher than the photoresponse signal, resulting in the low ON/OFF ratio and high signal noise of the device. Therefore, how to reduce the dark current to a lower level and retain excellent IR photodetection capabilities is a main obstacle that needs to be addressed for the practical applications of graphene photodetectors.

In this study, we develop an efficient graphene in-plane homogeneous p-n-p junction based IR photodetector with greatly reduced dark current. In the device, graphene is transferred onto SiO_2/Si substrate with multiple patterned silicon trenches, where graphene directly contacts with silicon substrate in silicon trenches. The graphene which directly contacts with the exposed silicon is found to be electron doped with a concentration of 2.4×10^{12} cm^{-2}, forming n-type graphene, while graphene on SiO_2 retains p-type doping. Highly efficient photodetection behaviors based on this in-plane homogeneous p-n-p junction are achieved over a broad wavelength region from infrared to mid-infrared (MIR) band (1.0–4.0 μm). It should be pointed out that a pristine graphene phototransistor with no silicon trenches in the channel region hardly responds to the MIR light. In our device, the light-activated functionality is provided by synergistic effects coming from the photovoltaic effects and photogating effects. In the graphene in-plane homogeneous p-n-p junctions, photo-generated holes are allowed to transfer out and extracted by the contact electrodes, whereas, electrons are trapped in the electron doped graphene. This photogating effect further induces carrier injection from the silicon substrate, enhancing the photoresponse performance. Noteworthy, it is found that this device architecture exhibits ultra-low dark current, i.e., $\sim10^{-9}$ A in double p-n-p junction architecture with two silicon trenches and $\sim10^{-13}$ A in three p-n-p junctions architecture with three silicon trenches. These findings offer a novel approach to design IR photodetectors and other optoelectronic devices based on 2D materials.

2 Device structure and working mechanism

Figure 1(a) shows the optical image of device. As shown in Figure 1(a), a Si/SiO_2 (300 nm) substrate with two silicon trenches is utilized as the substrate. The silicon trenches are defined with photolithography and etched by reactive iron etching (RIE) methods with a trench width, length and depth of 2 μm, 100 μm and 600 nm, respectively. Afterwards, the graphene is transferred and assembled onto the above substrate using a typical wet transfer method [29, 30]. The graphene contacting with SiO_2 surface and Si trench exhibits different doping states caused by silicon (in the silicon trenches) and absorbed chemicals (water or gas trapped in the SiO_2 surface [31]), respectively. To ascertain the doping level of pristine graphene on SiO_2 substrate, we fabricate the pristine graphene field-effect transistors (FETs) based photodetector on the Si/SiO_2 substrate and characterize the electrical performances. The transfer characteristics of the device under dark conditions are shown in Figure A1 in Appendix. The charge neutral point is located approximately at 19.2 V, and it means that most carriers are holes because of the doping effects coming from absorbed chemicals such as water or gas trapped in SiO_2 substrate and on the graphene film surface.

Figure 1(b) shows the Raman spectra of graphene films on different regions of the substrate collected to ascertain the quality and doping state of graphene films. The Raman characteristic peak shift is correlated with the change of charge density in graphene as previously reported. The upper panel of Figure 1(b) demonstrates the Raman spectrum of graphene on SiO_2 substrate. The result verifies the good quality and monolayer nature of graphene films on the SiO_2 surface ($I_{2\mathrm{D}}/I_{\mathrm{G}} > 2$). By comparison, the position of 2D peak in the lower panel is red-shifted slightly, indicating the increased electron concentration in the graphene film above the silicon trench. The 2D/G ratio of graphene on silicon decreases evidently compared with graphene on SiO_2 and it is concluded that the graphene on silicon region exhibits n-doping effects, according to the model developed by Das et al. [32]. Besides, the value of $I_{2\mathrm{D}}/I_{\mathrm{G}}$ is an important parameter to estimate the doping carrier density in graphene. The $I_{2\mathrm{D}}/I_{\mathrm{G}}$ value is calculated to be 2.79 and 1.81, respectively, corresponding to approximately 1.2×10^{12} cm^{-2} for hole doping in the graphene on SiO_2 and 2.4×10^{12} cm^{-2} for electron doping in the graphene on silicon trench, respectively. The chemical potential (μ) of graphene is the distance between charge neutrality point and Fermi level. We could also extract the chemical potential using the formula warning $\mu = \frac{h}{2\pi}\nu_F\sqrt{\pi n}$ [33], where warning $\nu_F = 10^6$ ms^{-1} is the Fermi velocity, n is the carrier density, and h is Planck's constant. The work function difference between the p-doped and n-doped graphene regions is calculated to be 53 meV.

To directly evaluate the band energy offset at the in-plane graphene p-n-p interface, Kelvin probe force

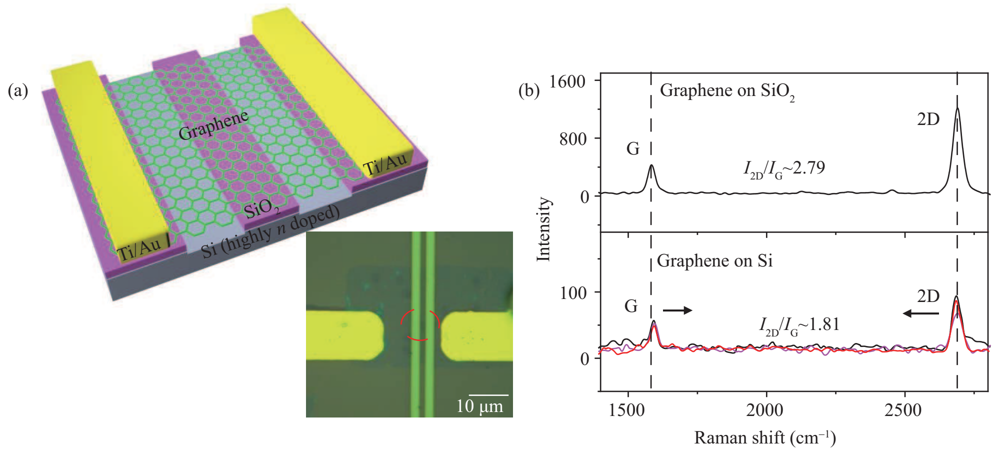

Figure 1 (Color online) The schematic diagrams and Raman spectra of photodetector based on graphene in-plane homogeneous p-n-p junctions. (a) Schematic of the device, bottom right: the optical image of device. (b) Raman spectra of the graphene film on different regions of the substrate.

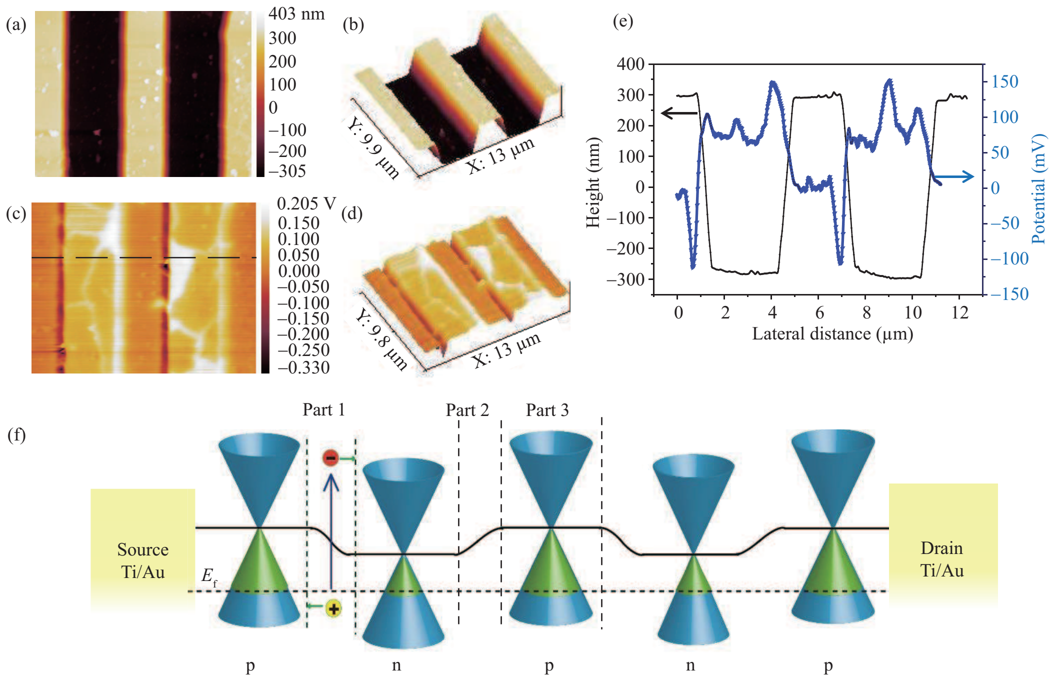

Figure 2 (Color online) The KPFM characterization and schematic band diagram of the device. (a), (b) The surface topographies of the device from 2D and 3D views. (c), (d) The surface potential distribution image of the device. (e) The height and potential profiles extracted from the dotted line in (c). (f) The schematic band diagram of the in-plane homogeneous graphene p-n-p junctions.

microscopy (KPFM) measurements are performed (Figure 2). Figures 2(a) and (b) show the surface topographies of the device from 2D and 3D views. The SiO_2 is removed thoroughly and the silicon etching depth reach 300 nm. Notably, as shown in Figures 2(c) and (d), an evident potential difference between graphene films on SiO_2 surface and silicon trenches is observed from the surface potential distribution image. The contact potential difference ($V_{\rm CPD}$) can reflect the difference in the work function between the probe tip and the surface of graphene, and the corresponding formula can be written as $V_{\rm CPD} = (W_{\rm probe} - W_{\rm graphene})/q$, where $W_{\rm probe}$ and $W_{\rm graphene}$ are the work function of probe tip and graphene surface, respectively. It is deduced that different $V_{\rm CPD}$ values reveal different work function of graphene films in different regions, and thus the work function difference can be calculated from the above equation. Figure 2(e) gives the height and potential profiles extracted from the dotted line in Figure 2(c), from which it can be obtained that $V_{\rm CPD}$ of n-type graphene on silicon trenches is higher than p-type graphene on SiO_2 surface, indicating higher work function of p-type graphene region than that of n-type graphene region. Notably, during the KPFM characterizations, the Kelvin probe is in direct contact with graphene films, and owing to the trench structure and some non-uniformity in graphene films, the surface potential distribution is non-uniform with some sharp ups and downs near the edge, as shown in Figure 2(e). We obtain the work function difference value of ~70 meV by taking the difference between potential values where the potential is relatively uniformly distributed. The small inconsistency between the work function difference obtained from Raman spectra and KPFM measurements is possibly owing to the non-uniform doping of graphene films or light illumination influence during KPFM measurements. The unavoidable light illumination during our KPFM measurements may induce slightly light doping in different graphene regions, and result in a possible work function difference compared to that in dark conditions. Nevertheless, the KPFM results provides a direct evidence for the formation of effective p-n junction between graphene films on the SiO_2 surface and silicon trenches, where the amount of in-plane homogeneous p-n junctions depends on the amount of silicon trenches. After contact, the Fermi levels in p- and n-type graphene region are aligned so as to satisfy the equilibrium condition and the build-in electric field is formed accompanying with energy band bending, which enables effective transportation of photo-carriers. Consequently, the schematic band diagram of in-plane homogeneous graphene p-n-p junctions can be depicted as illustrated in Figure 2(f). When the incident light with a beam spot diameter of around 2 μm is irradiated to the first junction area denoted by part 1 in Figure 2(f), the electron-hole pairs are generated immediately. Subsequentlly, the photo-carriers are separated by the built-in electrical fields and the holes are driven to the source electrode, while the electrons move to the opposite direction and are trapped in the n-doped region (graphene films on silicon trenches) owing to the potential barrier formed at part 2 of the structure. The trapped electrons in graphene act as a local gate and attract more holes from the bottom silicon substrate beneath the graphene film. This photogating effect further induces carrier injection from the silicon substrate to the graphene film, which in turn elevate the fermi energy of the n-doped graphene and thus increase the hole conductivity and the photocurrent, resulting in high responsivity of the device. Consequently, the synergistic effects of photovoltaic effect and photogating effect induce net photocurrent under short circuit condition.

3 Optoelectronic characterization and broadband photodetection behaviors

Next, we examine the photodetection behaviors of this in-plane homogeneous graphene p-n-p junctions based photodetector device. Figure 3(a) plots the characteristic drain-source current ($I_{\rm DS}$) in logarithmic plot versus drain-source voltage ($V_{\rm DS}$) of the device in dark and under 1064 nm IR light illumination at room temperature. Notably, the $I_{\rm DS}$-$V_{\rm DS}$ curve in Figure 3(a) is asymmetry in positive and negative voltage regions, different from the theoretical symmetry arising from the symmetric structure of device. The observed asymmetry between negative and positive voltage regions could be attributed to the uneven potential barrier distribution along the device channel induced by the non-uniform doping in graphene films or contact resistance. Under 1064 nm light illumination, the $I_{\rm DS}$-$V_{\rm DS}$ curve shifts upward and right slightly, implying the existence of photovoltaic effects. The photocurrent could be generated at zero external bias under 1064 nm light illumination as shown in Figure 3(b), which suggests the realization of a self-driven IR photodetector. At zero external bias, the photocurrent changes periodically when switching on and off the 1064 nm incident laser with different power ranging from 0.2 to 5.8 μW, and the largest photocurrent value of ~29 nA is obtained in the "on" state under 5.8 μW IR light illumination. It is worthy pointing out that good ON/OFF operation stability and reproducibility of the device can be achieved considering the photoresponse remains identical after several tens of switching cycles. The bias-dependent photoresponse of the device is also investigated at no external bias voltage in comparison with that under a bias voltage of 1 V under the same illumination conditions (Figure A2 in Appendix). The photocurrent at the bias voltage of 1 V increases remarkably, which is over three times higher than that at zero external bias. The external bias voltage induces an external electrical field in the in-plane graphene junction and then enlarges the built-in potential, which contributes to the transportation of photo-induced carriers and promotes the increase of photocurrent. This result offers the possibility of tuning the photoresponse of the device by applying an appropriate bias voltage. Moreover, the rise time and fall time of our photodetector (defined as the time required for the current transition from 10% to 90% and 90% to 10%, respectively) are found to be $\leqslant 53$ ms and $\leqslant 78$ ms, respectively (Figure 3(c)). This measured response speed value is not advantageous in comparison to other reported graphene junction based photodetectors owing to the limitations of the measurement setup in our experiments, and could

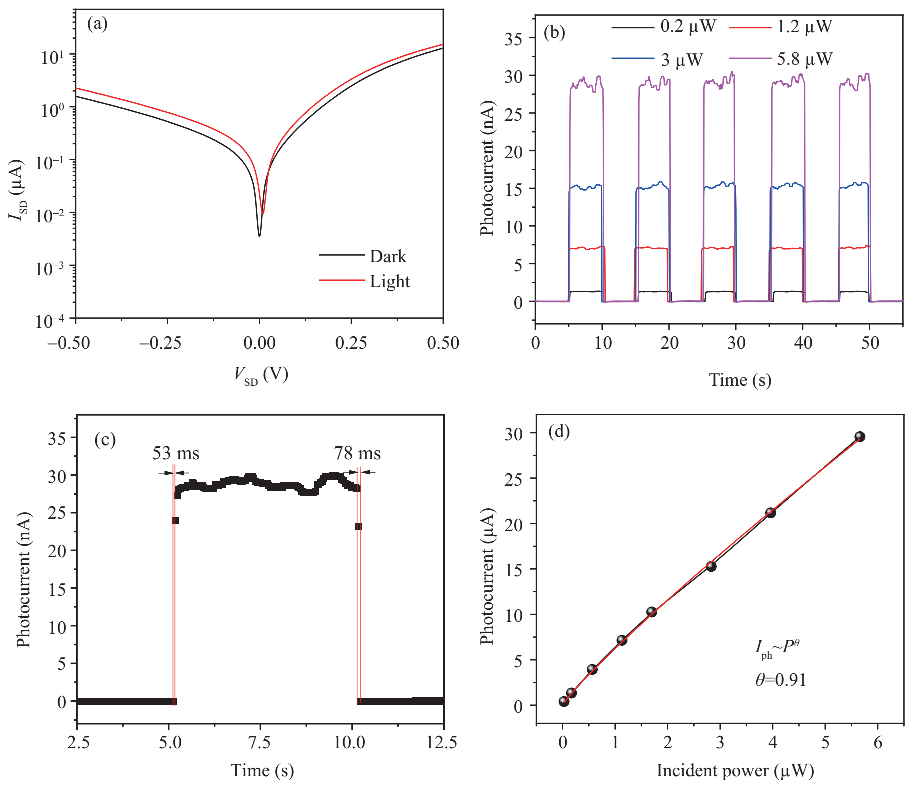

Figure 3 (Color online) Photodetection behaviors of the device under different incident powers. (a) The characteristic drain-source current in logarithmic plot versus drain-source voltage in dark and under 1064 nm IR light illumination at room temperature. (b) The photoresponse to periodical light pulses of device at zero external bias. (c) The rise time and the fall time of the device. (d) The dependence of photocurrent on illuminated light power at zero external bias voltage.

be characterized more precisely by combining more accurate analyzers. The photocurrent ($I_{\rm ph}$) as a function of light power intensity at zero external bias voltage is depicted in Figure 3(d). As we can see from the plot, the photocurrent increases steadily with the increase of light power ranging from 0.2 to 5.8 μW. The curve can be described by the power law, $I_{\rm ph} \sim P^{\theta}$, where θ is the exponent and determines the linearity of the photocurrent to light power. The value of θ is derived to be 0.91 by fitting the curve, implying the existence of few trap states and recombination current at low light power intensities.

To further assess the IR light detection capability of the device, we further carry out a series of photodetection measurements of the device at optical bands in the wavelength range of 1064–2200 nm. Figures 4(a) and (b) show the $I_{\rm DS}$ versus $V_{\rm DS}$ curve and corresponding temporal photoresponse characteristics under light illumination of different infrared wavelengths at the same laser power, respectively. The device exhibits obvious photoresponse to 1064–2200 nm IR light illumination, and rapid response/recovery to periodical light pulses. The key figure-of-merit of the photodetector, photoresponsivity (R), is given by $R = I_{\rm ph}/P_{\rm photo}$, where $P_{\rm photo}$ represents the light power illuminated on the active area of photodetector. Figure 4(c) shows the responsivity versus light power curves of the device. The largest responsivity is estimated to be around 14 mAW^{-1} under the 1064 nm incident light with a power of 0.03 μW. Importantly, our device can also operate effectively in MIR light region, which is beyond the response of intrinsic silicon. Figure 4(d) shows the self-driven photoresponse behaviors of the device under 4 μm MIR light irradiation. It is observed that the photocurrent changes periodically as the light source is switched on and off, and this ultra-wide spectrum detection capability of the device could expand its potential applications in mid-infrared light sensing. Notably, the response speed decreases obviously compared to that in shorter IR light wavelength regions, and we attribute this phenomenon to the thermal heating effects of graphene films, which could appear when graphene is irradiated by MIR lasers. It deserves further work to distinguish the dominant mechanism for the generation of photocurrent in MIR region in the graphene p-n-p junction photodetector.

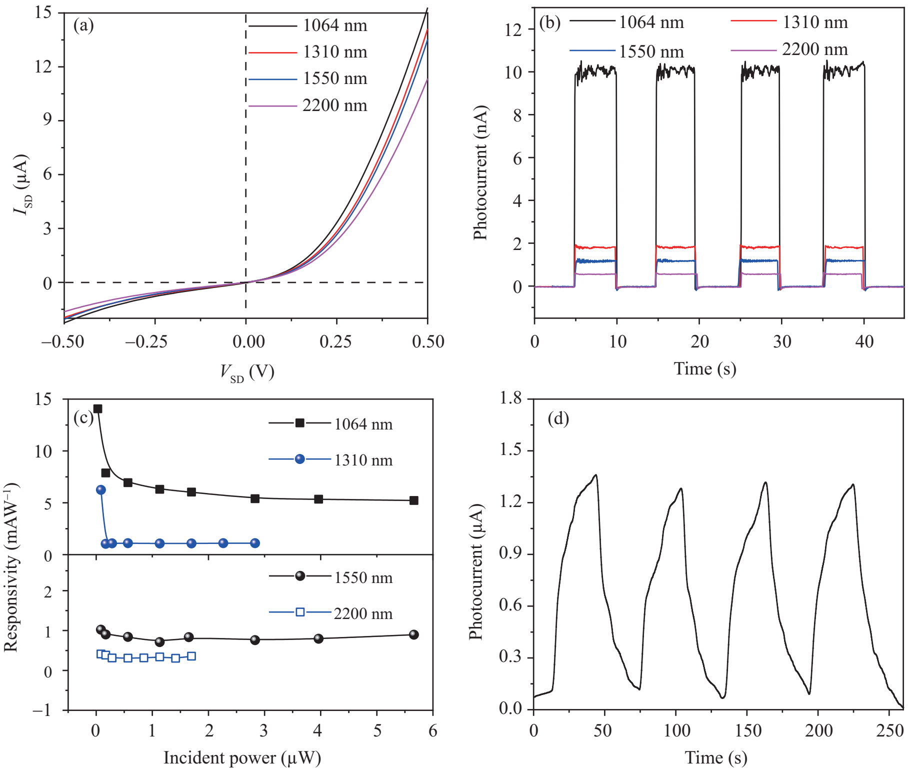

Figure 4 (Color online) The photodetection behaviors of the device under light illumination of different IR light wavelengths. (a) The drain-source current versus drain-source voltage curves. (b) The photocurrent response to periodical light pulses. (c) The responsivity versus light power curves of the device. (d) The self-driven photoresponse behaviors of the device under 4 μm MIR light irradiation.

4 Device dark current distribution

Interestingly, we found that our device architecture can effectively reduce the dark current. High dark current is a major contribution of noise current in graphene-based photodetectors, which will result in low signal-to-noise ratio (SNR) of the photodetectors. The term "dark current" is used to define the current flowing in the device in an all-black environment. We further transfer graphene onto SiO_2/Si substrate with three silicon trenches, and this device is formed by three p-n-p junctions. The distance between the two metal electrodes is the same as the device architecture we describe above. Figure 5(a) compares the dark currents of three different devices based on graphene device on SiO_2 substrate with no silicon trenches, graphene device on SiO_2 substrate with two silicon trenches and three silicon trenches, respectively. The width and length of the device channel are 100 μm and 20 μm, respectively. Notably, the photodetector device on SiO_2 substrate with two silicon trenches and three silicon trenches exhibits an ultra-low dark current of 10^{-9} A and 10^{-13} A, respectively, which is almost three and seven orders of magnitude lower than that of the pristine graphene phototransistor and the device on SiO_2 substrate with no silicon trenches, respectively. Importantly, the dark current of our device architecture is comparable to or lower than the dark current value in previous reported graphene homojunction based photodetectors [26–28, 34–38]. The major sources of dark current are thermal generation of carriers and diffusion current of minority carriers in our device architecture. When the device is operated under bias voltage, thermal-generated holes move toward the source electrode, and the n-doped graphene region leads to majority of electric field drop which allows unimpeded flow of holes, meanwhile acts as electron barrier blocking the minority carrier diffusion from carriers-generated region into the drain electrode and hence reduces the dark current. The specific detectivity (D^*) is a figure of merit to measure the sensitivity in photodetectors and it can be expressed as follows: $D^* = R\sqrt{A}/\sqrt{2qI_{\rm dark}}$, D^* is calculated to be 2.87×10^8 cm·Hz$^{1/2}$·W^{-1} in graphene based double p-n-p junctions (1 V bias voltage, 1064 nm light, 0.56 μW). Figure 5(b) gives the photocurrent comparisons of the devices based on double graphene p-n-p junction and three p-n-p junctions on SiO_2 substrate as a function of light power, respectively. The photocurrent in both devices is almost proportional to the light power ranging from 0.2 to 4 μW,

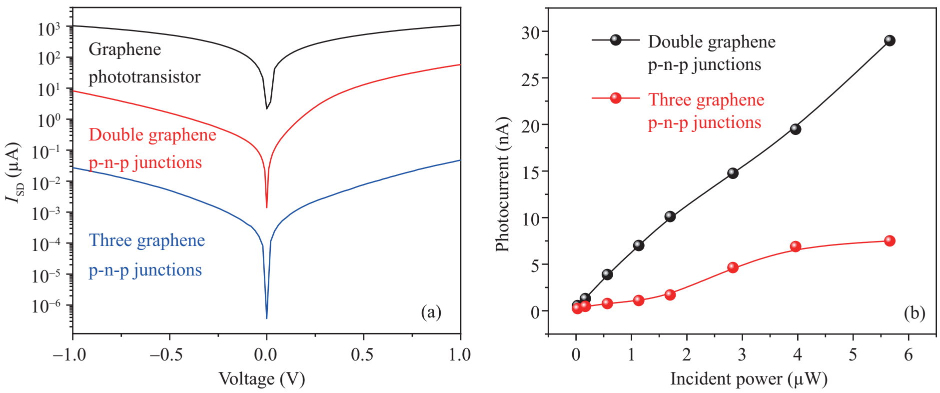

Figure 5 (Color online) Photodetection behaviors of the device based on different structures. (a) The dark currents of three different devices. (b) The photocurrent comparisons of different devices.

however, it becomes close to be saturated in the photodetector based on three p-n-p junctions on SiO_2 substrate when the light power is further increased. This could be attributed to the increased defect states in graphene films.

5 Conclusion

In summary, we proposed an effective route for reducing the dark current of graphene photodetector by transferring the CVD-growth graphene films onto the patterned Si/SiO_2 substrates. The device based on the in-plane homogeneous graphene p-n-p junctions exhibits excellent photoresponse to IR lights with greatly reduced dark current. It is worth pointing out that this in-plane homogeneous graphene p-n-p junction based photodetector device can operate effectively into the mid-infrared wavelength region. It is also found that this device architecture can reduce the dark current to be several orders of magnitude lower than pristine graphene phototransistors. The excellent IR photodetection capabilities could be attributed to the different doping effects of graphene attached to Si and SiO_2 substrates and the formation of in-plane homogeneous graphene p-n-p junctions, as well as the photogating effect induced carrier injection from the silicon substrate. The achievement of this in-plane homogeneous graphene p-n-p junction based IR photodetectors will offer exciting opportunities for the creation of graphene-silicon integrated broadband optical devices. Further improvements over the device structure are possible, such as increasing the potential difference of graphene in different region by chemical doping, optimizing the number of stacks by additional light absorbing layers.

Acknowledgements This work was supported by National Natural Science Foundation of China (Grant Nos. 62022081, 61974099, 61705152, 61604102), National Key Research & Development Program (Grant Nos. 2016YFA0201900, 2016YFA0201902), Open Foundation of State Key Laboratory of Electronic Thin Films and Integrated Devices (Grant No. KFJJ202002), and Collaborative Innovation Centre of Suzhou Nano Science & Technology.

References

1 Tielrooij K J, Piatkowski L, Massicotte M, et al. Generation of photovoltage in graphene on a femtosecond timescale through efficient carrier heating. Nat Nanotech, 2015, 10: 437–443
2 Du X, Skachko I, Barker A, et al. Approaching ballistic transport in suspended graphene. Nat Nanotech, 2008, 3: 491–495
3 Geim A K. Graphene: status and prospects. Science, 2009, 324: 1530–1534
4 Zhang Y Z, Liu T, Meng B, et al. Broadband high photoresponse from pure monolayer graphene photodetector. Nat Commun, 2013, 4: 1811
5 Liu C-H, Chang Y-C, Norris T B, et al. Graphene photodetectors with ultra-broadband and high responsivity at room temperature. Nat Nanotech, 2014, 9: 273–278
6 Wang X, Cheng Z, Xu K, et al. High-responsivity graphene/silicon-heterostructure waveguide photodetectors. Nat Photon, 2013, 7: 888–891
7 Youngblood N, Anugrah Y, Ma R, et al. Multifunctional graphene optical modulator and photodetector integrated on silicon waveguides. Nano Lett, 2014, 14: 2741–2746
8 Xia F, Mueller T, Lin Y M, et al. Ultrafast graphene photodetector. Nat Nanotech, 2009, 4: 839–843
9 Mueller T, Xia F, Avouris P. Graphene photodetectors for high-speed optical communications. Nat Photon, 2010, 4: 297–301
10 Bae S, Kim H, Lee Y, et al. Roll-to-roll production of 30-inch graphene films for transparent electrodes. Nat Nanotech, 2010, 5: 574–578
11 Li X, Cai W, An J, et al. Large-area synthesis of high-quality and uniform graphene films on copper foils. Science, 2009, 324: 1312–1314
12 Weiss E, Klin O, Grossmann S, et al. InAsSb-based XB_nn bariodes grown by molecular beam epitaxy on GaAs. J Cryst Growth, 2012, 339: 31–35
13 Yin J, Paiella R. Multiple-junction quantum cascade photodetectors for thermophotovoltaic energy conversion. Opt Express, 2010, 18: 1618–1629

14 Lemme M C, Koppens F H L, Falk A L, et al. Gate-activated photoresponse in a graphene p-n junction. Nano Lett, 2011, 11: 4134–4137
15 Seo B H, Youn J, Shim M. Direct laser writing of air-stable p-n junctions in graphene. ACS Nano, 2014, 8: 8831–8836
16 Kim S, Shin D H, Kim C O, et al. Graphene p-n vertical tunneling diodes. ACS Nano, 2013, 7: 5168–5174
17 Tian P, Tang L, Teng K S, et al. Recent advances in graphene homogeneous p-n junction for optoelectronics. Adv Mater Technol, 2019, 4: 1900007
18 Lin L, Liao L, Yin J, et al. Building graphene p-n junctions for next-generation photodetection. Nano Today, 2015, 10: 701–716
19 Herring P K, Hsu A L, Gabor N M, et al. Photoresponse of an electrically tunable ambipolar graphene infrared thermocouple. Nano Lett, 2014, 14: 901–907
20 Oh H, Coh S, Son Y-W, et al. Inhibiting Klein tunneling in a graphene p-n junction without an external magnetic field. Phys Rev Lett, 2016, 117: 016804
21 Brun B, Moreau N, Somanchi S, et al. Imaging Dirac fermions flow through a circular Veselago lens. Phys Rev B, 2019, 100: 041401
22 D'Arsié L, Esconjauregui S, Weatherup R S, et al. Stable, efficient p-type doping of graphene by nitric acid. RSC Adv, 2016, 6: 113185–113192
23 Xie Z, Yao R, Zhang Y, et al. Effect of Au_2Cl_6 doping on stability and work function of graphene. Phys B-Condens Matter, 2019, 558: 1–4
24 Liang C, Wang Y, Li T. Synthesis of sulfur-doped p-type graphene by annealing with hydrogen sulfide. Carbon, 2015, 82: 506–512
25 Chiu H-Y, Perebeinos V, Lin Y-M, et al. Controllable p-n junction formation in monolayer graphene using electrostatic substrate engineering. Nano Lett, 2010, 10: 4634–4639
26 Liu N, Tian H, Schwartz G, et al. Large-area, transparent, and flexible infrared photodetector fabricated using p-n junctions formed by n-doping chemical vapor deposition grown graphene. Nano Lett, 2014, 14: 3702–3708
27 Kim C O, Kim S, Shin D H, et al. High photoresponsivity in an all-graphene p-n vertical junction photodetector. Nat Commun, 2014, 5: 3249
28 Wang S, Sekine Y, Suzuki S, et al. Photocurrent generation of a single-gate graphene p-n junction fabricated by interfacial modification. Nanotechnology, 2015, 26: 385203
29 Suk J W, Kitt A, Magnuson C W, et al. Transfer of CVD-grown monolayer graphene onto arbitrary substrates. ACS Nano, 2011, 5: 6916–6924
30 Chen Y, Gong X-L, Gai J-G. Progress and challenges in transfer of large-area graphene films. Adv Sci, 2016, 3: 1500343
31 Liu Y, Shivananju B N, Wang Y, et al. Highly efficient and air-stable infrared photodetector based on 2D layered graphene-black phosphorus heterostructure. ACS Appl Mater Interfaces, 2017, 9: 36137–36145
32 Das A, Pisana S, Chakraborty B, et al. Monitoring dopants by Raman scattering in an electrochemically top-gated graphene transistor. Nat Nanotech, 2008, 3: 210–215
33 Novoselov K S, Geim A K, Morozov S V, et al. Two-dimensional gas of massless Dirac fermions in graphene. Nature, 2005, 438: 197–200
34 Sun T, Wang Y, Yu W, et al. Flexible broadband graphene photodetectors enhanced by plasmonic $Cu_{3-x}P$ colloidal nanocrystals. Small, 2017, 13: 1701881
35 Latorre-Sánchez M, Primo A, Atienzar P, et al. p-n heterojunction of doped graphene films obtained by pyrolysis of biomass precursors. Small, 2015, 11: 970–975
36 Wang G, Zhang M, Chen D, et al. Seamless lateral graphene p-n junctions formed by selective in situ doping for high-performance photodetectors. Nat Commun, 2018, 9: 5168
37 Yu X C, Shen Y D, Liu T, et al. Photocurrent generation in lateral graphene p-n junction created by electron-beam irradiation. Sci Rep, 2015, 5: 12014
38 Lin L, Xu X, Yin J B, et al. Tuning chemical potential difference across alternately doped graphene p-n junctions for high-efficiency photodetection. Nano Lett, 2016, 16: 4094–4101

Appendix A

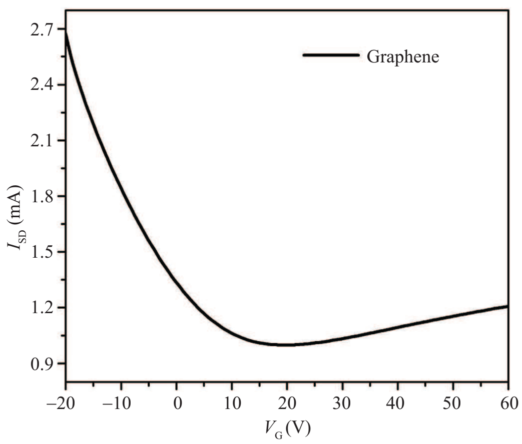

Figure A1 Transfer characteristics of the pristine graphene transistor on SiO_2/Si substrate under dark condition.

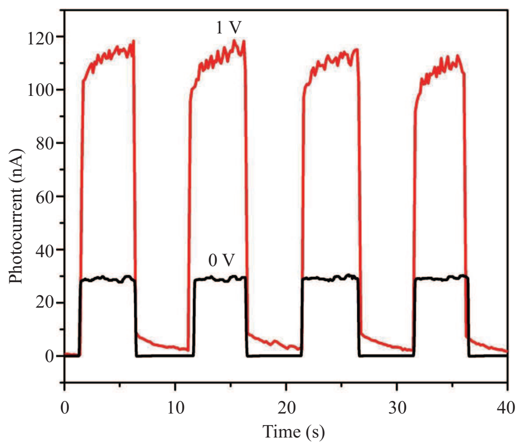

Figure A2 (Color online) The photoresponse of the device under different bias voltages.